EFFECT OF DIELECTRIC BARRIER DISCHARGE PLASMA ON FILM COOLING PERFORMANCE

by

Jie SUN[a], Fuxing ZHANG[a], Jin WANG[a,b*], Jakov BALETA[c], Gongnan XIE[d], and Bengt SUNDEN[e*]

[a] School of Energy and Environmental Engineering, Hebei University of Technology, Tianjin, China
[b] Key Laboratory of Thermo-Fluid Science and Engineering (Xi'an Jiaotong University), Ministry of Education, Xi'an, China
[c] Faculty of Metallurgy, University of Zagreb, Sisak, Croatia
[d] Northwestern Polytechnical University, Xi'an, China
[e] Department of Energy Sciences, Division of Heat Transfer, Lund University, Lund, Sweden

Original scientific paper
https://doi.org/10.2298/TSCI2205157S

To improve film cooling effectiveness of a gas turbine blade, a kind of plasma actuator is introduced on the blade surface. The effect of three arrangements of plasma actuators on flow characteristics and film cooling performance is numerically investigated by a verified turbulence model. Results show that the coolant air under plasma is pulled down to the wall, and the near-wall air is sped up to promote the film cooling effectiveness downstream the wall. It is discovered that the plasma actuators near the film hole show weaker aerodynamic actuation than that downstream the wall. Compared with the plasma actuators off case, the maximum improvement in the wall-averaged film cooling effectiveness of the case with up plasma actuators is 11.7% under low blowing ratios. The wall-averaged film cooling effectivenesses of the cases with down plasma actuators and up-down plasma actuators increase by 138.3% and 122.9% under the blowing ratio of 1.5.. Vortex structures are broken up, and vortex is separated by two jets induced by aerodynamic actuation. The maximum wall pressure difference reaches 1.89% when plasma actuator is arranged downstream the wall.

Key words: *aerodynamic actuation, film cooling, flow control, gas turbine, plasma arrangement*

Introduction

Inlet temperature of gas turbine above 1800 K is exceeding melting temperature of blade materials (about 1500 K) [1]. Growth rate of inlet temperature for gas turbines is significantly higher than development rate of temperature-resistant materials [2]. As one of the most common and effective external cooling methods, film cooling was used to avoid damages of components in advanced gas turbines by gas in high temperature [3]. The coolant air emitted from discrete holes is suppressed towards blade surfaces by high pressure gas, and a layer of air film in low temperature is formed over the blade surfaces [4].

Tian *et al.* [5] analyzed effect of combined hole on film cooling numerically. Results showed that film cooling effectiveness from combined hole was higher than that from cylindrical hole at blowing ratio of 0.25-1.5. Ravi *et al.* [6] found that average film cooling effec-

* Corresponding authors, e-mails: wjwcn00@163.com, bengt.sunden@energy.lth.se

tiveness on cascade end-wall with a semi-cylindrical trench increased by 30.4% compared to that without trench. Recently, some researchers have focused on performance of plasma actuators on film cooling. As one new device for flow control, plasma actuators had some advantages, such as fast response, small volume and low power consumption [7]. Compared with other flow control methods, plasma actuation showed obvious advantages in controlling the flow field by ionized air to form plasma [8]. Audier *et al.* [9] investigated effect of surface dielectric barrier discharge (SDBD) driver on heat transfer downstream a slot. Results showed that regardless of the blowing ratios, the actuator induced the coolant air to deflect towards the wall, which delayed lateral diffusion of the coolant jet. Dai *et al.* [10] investigated effect of plasma induction on a round jet using smoke visualization method. Results showed that normal height of the coolant air increased when the applied voltage decreased from 14 kV to 0 kV. Li *et al.* [11] studied an effect of a saw-tooth plasma actuator (STPA) on film cooling by adopting large eddy simulation method. Consequences showed that the cooling effectiveness in the case with STPA-on-tip was 28.1% lower than that with STPA-off.

The SDBD plasma actuation can effectively restrain flow separation by inducing airflow. Due to aerodynamic actuation of plasma, the coolant air adheres to blade surface, which effectively reduces temperature on blade surface [12]. Zhang *et al.* [13] experimentally studied control effect of DBD plasma on airfoil flow separation. Results showed that the plasma actuation at low voltage amplitude resulted in a laminar jet, whereas the increase in voltage amplitude plasma jet changed into a turbulent jet. Using particle image velocimetry and laser doppler velocimetry, Schatzman *et al.* [14] conducted plasma flow control experiments about boundary-layer separation of adverse pressure gradient. Results showed that the stable spreading drive produced the wall-jet effect, which increased the near-wall momentum. The slope surface pressure coefficient increased by 53% under 40 kV applied voltage. Hu *et al.* [15] studied an effect of dual-electrode DBD plasma actuator on a rotor blade. Results showed that area of flow separation decreased significantly at rotation speed of 300 rpm, and the phenomenon of the flow separation disappeared at 1200 rpm when the plasma actuator was applied.

Although many studies have focused on the effect of plasma actuator on flow control, few discussions on the application of plasma were involved with convective heat transfer enhancement. The effects of plasma actuator position on film cooling and pressure loss have been discussed insufficiently. Based on the plasma phenomenology method mentioned by Shyy *et al.* [16], the electric body force of the plasma was coupled to the momentum equation as a source term. Film cooling performance of flat plate will be investigated numerically by changing the arrangement of plasma actuators. The flow field disturbance and heat transfer enhancement are studied by analyzing the effect of plasma actuator on 3-D vortex structures. These results provide a research foundation for optimizing the number and action intensity of plasma actuation in active flow control, which is an important reference for enhancing film cooling using plasma actuators.

Model validation

A model validation is conducted by comparisons between present results and published data.

Model geometry and plasma actuator

Cylindrical hole with diameter of 12.7 mm (D) is used in present simulations. The hole has an inclined angle of 35° and length (L) of 4D. Mainstream access has length of 59D, height of 10D and width of 3D as shown in fig. 1. It is a distance of 19D between the main-

stream inlet and the hole outlet. The coolant chamber has dimensions of $6D \times 6D \times 3D$. The origin of coordinates is situated in the trailing edge of film hole outlet. The axes X, Y, and Z are streamwise direction, spanwise direction and normal direction in the computational domain.

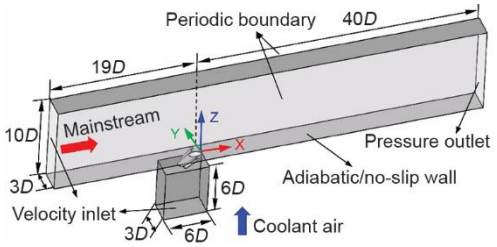

Figure 1. Diagrammatic drawing of the computational domain

Figure 2 shows four arrangements of plasma actuators (PA) on the bottom wall, that is, PA-off, PA-up, PA-down and PA-both cases. In PA-off and PA-up cases, the leading edges of the exposed electrodes are located at $X = 0$ and $X = 8D$ as shown in figs. 2(b) and 2(c). The leading edges of two exposed electrodes in fig. 2(d) are located at $X = 0$ and $X = 8D$. Both exposed and covered strip electrodes are arranged asymmetrically on both sides of the wall. Table 1 shows the parameters of the plasma actuator. The width of the exposed electrode, L_1, was 5 mm, and the covered electrode, L_2, was 10 mm. The spanwise length, L_3, of both is $3D$. The streamwise direction distance, s, between the two electrodes is 0.5 mm and the thickness, h, of the electrode is 0.1 mm.

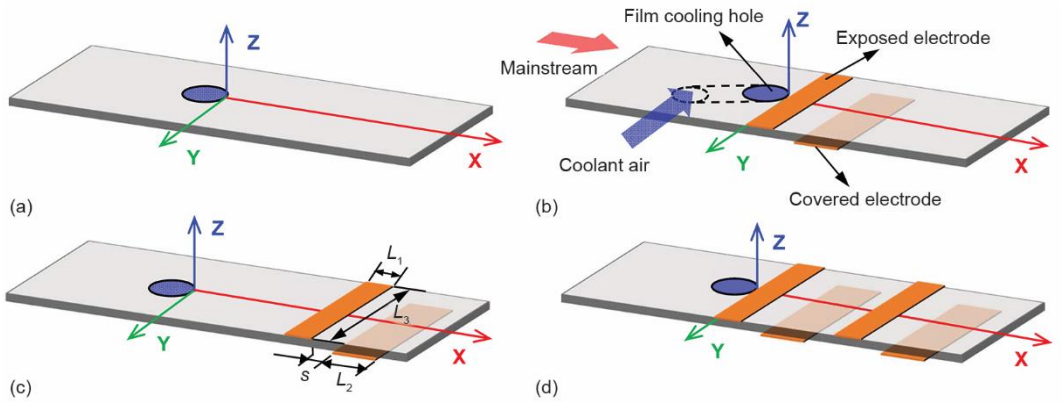

Figure 2. Arrangements of plasma actuators; (a) PA-off, (b) PA-up, (c) PA-down, and (d) PA-both

Boundary conditions

Boundary conditions for present simulations are seen in tab. 2. The mainstream and coolant air are presumed to be ideal gases, and both inlets are set as velocity-inlet boundary conditions. The inlet temperature of mainstream, T_∞, with velocity, U_∞, of 20 m/s is 300 K, and the inlet temperature of coolant air, T_c, is 200 K in numerical calculations. The mainstream outlet is the pressure-outlet boundary condition at a pressure of 101325 Pa. The density ratio, DR, of the mainstream to the coolant air is 1.5. Two side walls of mainstream channel and coolant chamber are periodic boundary, and else walls are set as adiabatic and no-slip boundary conditions. The height of the first layer grid over the channel wall is $0.001D$, and the growth rate of grids is 1.1.

Governing equations

Figure 3 shows diagrammatic drawing of plasma aerodynamic actuation and phenomenological model. The plasma actuator is constituted by an exposed electrode and a cove-

Table 1. Parameters of plasma actuator

Parameters	Values
Vertical height of the plasma area, a	3 mm
Streamwise length of the plasma area, b	6 mm
Width of exposed electrode, L_1	5 mm
Width of covered electrode, L_2	10 mm
Spanwise length of the electrode, L_3	3D
Spacing between the electrodes, s	0.5 mm
Thickness of two electrodes	0.1 mm

Table 2. Boundary conditions

Parameters	Values
Temperature of mainstream inlet, T_∞	300 K
Inlet velocity of mainstream, U_∞	20 m/s
Outlet pressure	101325 Pa
Temperature of coolant air inlet, T_c	200 K
Density ratio, DR	1.5

red electrode. The air above the covered electrode is ionized to generate a non-thermal plasma layer when high frequency and high voltage alternating current are applied to both ends of electrodes. The electric field results in momentum exchanges due to collision of charged particles and surrounding air molecules. Under plasma actuation, the coolant air near the wall is speeded up and pulled down to the wall, which enhances the attachment ability of the coolant air to the wall. The phenomenological model mentioned by Shyy *et al.* [16] neglected collision between charged particles and air molecules, and the plasma is generated in the triangular region AOB as seen in fig. 3(b).

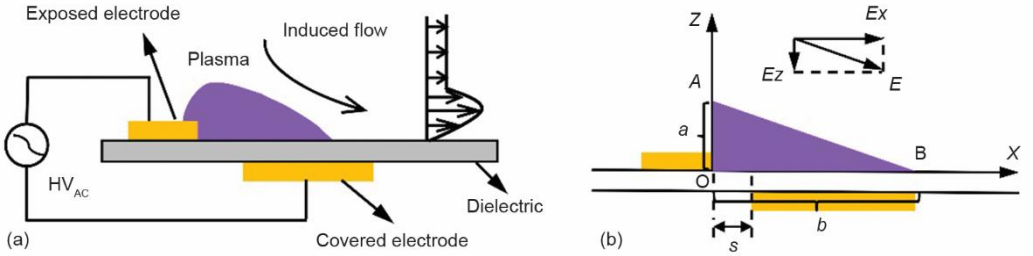

Figure 3. Diagrammatic drawing of plasma aerodynamic actuation and phenomenological model; (a) plasma actuator and (b) phenomenological model

Intensity of electric field decreases linearly along coordinate axis, and it is expressed as according to [16]:

$$E(X,Z) = \left|\vec{\mathrm{E}}\right| = E_0 - k_1 X - k_2 Z \tag{1}$$

$$k_1 = \frac{E_0 - E_\mathrm{b}}{b} \tag{2}$$

$$k_2 = \frac{E_0 - E_\mathrm{b}}{a} \tag{3}$$

where E_0 represents the ratio of applied voltage, φ_0, to electrode gap, s, k_1 and k_2 are spatial distribution coefficients of electric field intensity, which represents the spatial distribution gradient of electric field intensity. The breakdown electric field intensity, E_b, is 30 kV/cm in

present simulations. The constituents of the electric field in the directions X and Z are given by:

$$E_x(X,Z) = \frac{Ek_2}{\sqrt{k_1^2 + k_2^2}} \tag{4}$$

$$E_z(X,Z) = \frac{Ek_1}{\sqrt{k_1^2 + k_2^2}} \tag{5}$$

where the body force constituents in the directions X and Z are:

$$F_X = \rho_c e_c f \Delta t E_X \tag{6}$$

$$F_Z = \rho_c e_c f \Delta t E_Z \tag{7}$$

where the charge density, ρ_c, is 10^{17} C/m^3, and the elementary charge e_c is 1.6×10^{-19} C, f is the frequency of applied voltage, and duration of plasma actuation, Δt, is 67 μs. More details are seen in [16].

The electric body force of the plasma is taken as the source term of the steady body force, which is added into the momentum equation through the user-defined functions of ANSYS FLUENT 18.0. The applied frequency in this research is 3 kHz.

In the present study, the blowing ratio, M, is calculated by [17]:

$$M = \frac{\rho_c U_c}{\rho_\infty U_\infty} = DR\frac{U_c}{U_\infty} \tag{8}$$

where DR is density ratio of coolant air to mainstream, ρ – the density, and U – the flow velocity. The c presents coolant air, and ∞ – the mainstream. The film cooling effectiveness is defined:

$$\eta = \frac{T_\infty - T_{aw}}{T_\infty - T_c} \tag{9}$$

where T_∞ represents the inlet temperature of mainstream, T_c – the inlet temperature of coolant air, and T_{aw} – the wall temperature. The average film cooling effectiveness is calculated by:

$$\bar{\eta} = \frac{T_\infty - \overline{T_{aw}}}{T_\infty - T_c} \tag{10}$$

where $\overline{T_{aw}}$ represents average wall temperature. The dimensionless temperature is:

$$\Theta = \frac{T_{aw}}{T_\infty} \tag{11}$$

where U is the streamwise velocity and W is the normal velocity. The dimensionless average film cooling effectiveness is expressed:

$$\Gamma = \frac{\bar{\eta}}{\eta_0} \tag{12}$$

where $\overline{\eta}_0$ represents spanwise average film cooling effectiveness of referenced case. The expression of Q criterion is used to identify 3-D vortex structures in a flow field, and it is defined [18]:

$$Q = -\frac{1}{2}\left[\left(\frac{\partial u}{\partial x}\right)^2 + \left(\frac{\partial v}{\partial y}\right)^2 + \left(\frac{\partial w}{\partial z}\right)^2\right] - \frac{\partial u}{\partial y}\frac{\partial v}{\partial x} - \frac{\partial u}{\partial z}\frac{\partial w}{\partial x} - \frac{\partial v}{\partial z}\frac{\partial w}{\partial y} \tag{13}$$

Grid independence analysis and model validation

Enhanced wall function is used for numerical simulations. The near-wall meshes are refined to capture the complex flow phenomena near the wall. Figure 4 presents film cooling effectiveness on the centerline for cases with 0.65, 1.30, and 2.60 million cells. The cooling effectiveness curves with the grid numbers of 1.30 million and 2.60 million almost overlap with average error of 0.2%. However, the average error between results from 0.65 million and 1.30 million grid numbers is 1.4%. Therefore, the grid number of 1.30 million is used in present simulations.

In our previous study [19], results from realizable k-ε model, standard k-ε model and RNG k-ε model were compared with data in Sinha *et al.* [20]. Based on standard k-ε model, fig. 5 reveals centerline film cooling effectiveness along streamwise direction has the same trend as that in Sinha *et al.* [20], corresponding to a minimum average error of 2.0%. The average errors between other turbulence models and experimental data of Sinha *et al.* [20] are above 10%. Therefore, the standard k-ε turbulence model is chosen in this paper.

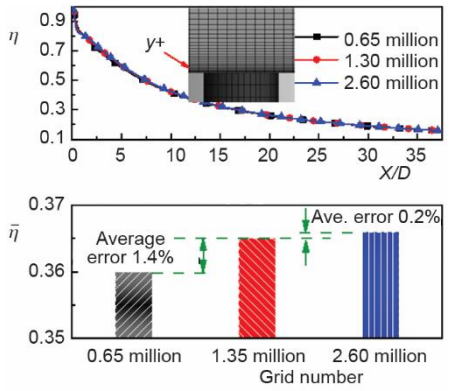

Figure 4. Analysis of grid independence

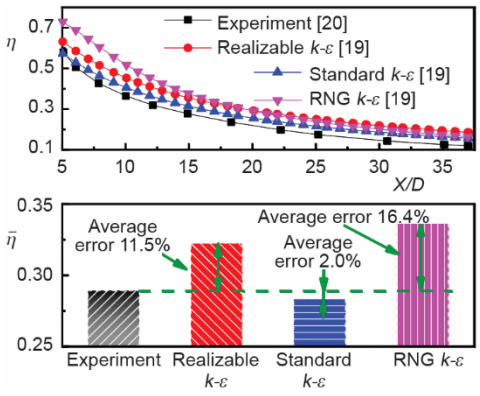

Figure 5. Validation of turbulence model

Dimension of model validation is 21.5×10 mm. Applied voltage and frequency of plasma actuator are 4 kV and 3 kHz. Figure 6 shows comparisons of near-wall streamwise velocities between present numerical results and results in Shyy *et al.* [16]. Since the specific settings of [16] are not given, the calculation speed of this study is relatively large. However, the maximum induced velocity in present research at X = 17.3 mm is close to that in [16], and the average errors between results in this study and in [16] are 8.8% and 1.7% at inlet velocities of 2 m/s and 5 m/s. These results manifest that the plasma actuation model is reliable and reasonable.

Results and discussion

With different plasma arrangements, fig. 7 shows streamlines and dimensionless temperature contours in different spanwise sections X/D = 2, 5 and 10. In the case with plasma off (PA-off), streamlines over the wall have the maximum height in the whole streamwise direction compared to the results in the case with plasma actuation. When the plasma actuator is arranged nearby the hole outlet (PA-up case), the coolant air is pressed towards the wall at around $X = 3D$. This is because plasma aerodynamic actuation reduces outlet momentum of coolant air, which enhances the adhesion effect. More significant adhesion effect is observed, when two plasma actuators are located close to the hole and downstream the wall (PA-both case). It is clearly seen from figs. 7(c)-7(d) that the coolant air is pulled down to the wall surface near the X/D = 8, which causes a large low temperature zone downstream the wall. This result is because the flow velocity downstream the coolant air is lower than that at hole outlet, and the plasma actuator is easier to control the flow distribution in low speed.

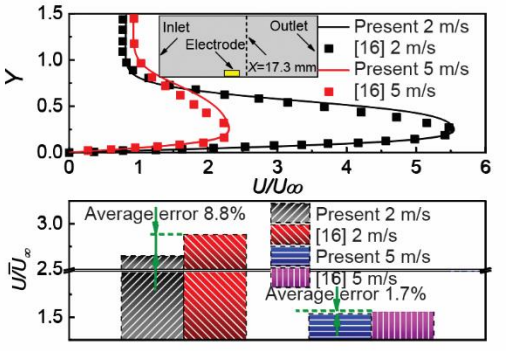

Figure 6. Velocity distributions under different inlet velocities at X = 17.3 mm

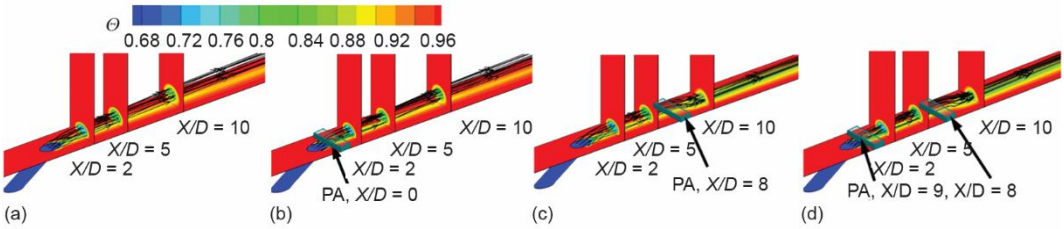

Figure 7. Streamlines and dimensionless temperature contours of different spanwise sections (X/D = 2, 5, 10) in different plasma arrangements, M = 1.0; (a) PA-off, (b) PA-up, (c) PA-down, and (d) PA-both

Figure 8 shows dimensionless velocity contours at streamwise locations of $X = 2D$ and $10D$. The U/U_∞ represents dimensionless streamwise velocity, and W/U_∞ is dimensionless normal velocity. Flow velocity close to the wall with plasma actuation is significantly higher than without plasma, and the maximum induced velocity is three times that of the mainstream velocity. At the same cross section, velocity boundary layer near the wall gets thinner when plasma actuator is applied. This result shows the pull-down effect of plasma on the coolant air. At the section of $X = 2D$, the normal velocity without plasma is higher than that with plasma at

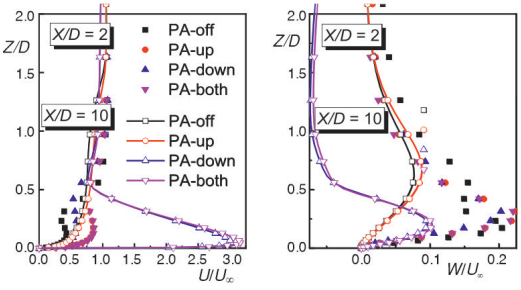

Figure 8. Comparisons of dimensionless velocity at different streamwise locations

the same position, which indicates that coolant air has a strong ability to penetrate the mainstream due to plasma actuation. At the section of $X = 10D$, the normal velocity in the PA-down and PA-both cases at $Z > 0.4D$ is smaller than that in the PA-off case. The largest normal velocity is observed in the PA-up case. This is because the PA-up has a limited control over air flow, and most of energy is used to offset large outlet momentum of coolant air. It shows that the effect of the PA-down is more obvious under blowing ratio of 1.0.

Figure 9 presents film cooling effectiveness contours downstream the wall in different arrangements of actuators. Compared with PA-off case, the film cooling effectiveness distribution along the streamwise direction in PA-up case is higher than those under low blowing ratios ($M = 0.25$ and 0.5). The area near the cooling hole shows high film cooling effectiveness, which manifests that the plasma shows the wall-jet effect on the coolant flow. The film cooling effectiveness in PA-down and PA-both cases downstream $X = 10D$ shows higher values compared to else cases under high blowing ratios, whereas the cooling effectiveness distributions both along the streamwise direction and the spanwise direction in the PA-up case are higher than those in else cases under low blowing ratios. This is because the normal velocity of the coolant air is small under low blowing ratios, and the aerodynamic actuation of the plasma results in rebound of fluid near the wall. Under high blowing ratios, the arrangement of the plasma actuator at $X/D = 8$ promotes the film cooling performance of the whole downstream wall. These consequences reveal that the arrangement of the plasma actuator has significant influence on improvement of film cooling effectiveness under different blowing ratios.

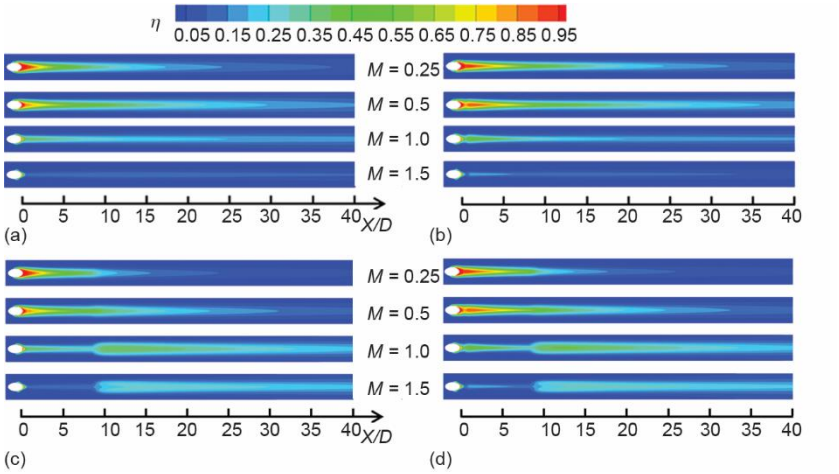

Figure 9. Wall contours of film cooling effectiveness for various actuator arrangements; (a) PA-off, (b) PA-up, (c) PA-down, and (d) PA-both

Comparisons of spanwise average film cooling effectiveness, $\bar{\eta}$, and dimensionless spanwise average effectiveness, Γ, downstream the wall are conducted by considering various arrangements of actuators as shown in fig. 10. The largest gradient is nearby the cooling hole, and the average film cooling effectiveness of PA-off decreases gradually along the spanwise direction. This is because the momentum and inertia of the coolant air show somewhat effect on the flow distribution near the outlet. The best film cooling performance is reached at the blowing ratio of 0.5. The PA-up case shows higher average cooling effectiveness in the streamwise direction than that PA-off, and the maximum film cooling effectiveness increases by 22.2% and 21.9% under low blowing ratios of 0.25 and 0.5. The cooling effectiveness near

the cooling hole increases by 34.0% and 45.9% under high blowing ratios of 1.0 and 1.5. The fluid near the actuator is accelerated and pulled down by the wall-jet action of the plasma, whereas the fluid far away from the actuator is lifted off the wall and mixed by the mainstream due to the reduction of the momentum. As shown in fig. 10(c), the cooling effectiveness in the PA-down case has the maximum increases of 98.2% and 180.2% under high blowing ratios of 1.0 and 1.5, whereas the ones in the PA-down case have the maximum increases of 2.5% and 3.7% under low blowing ratios of 0.25 and 0.5. This result is because the coolant air downstream the actuator bounces off the wall at low blowing ratios. As shown in fig. 10(d), the average cooling effectiveness of PA-both increases by 21.4%, 22.4%, 91.8%, and 159.6% under the four blowing ratios. This result indicates that the arrangement of the actuator has a significant effect on improving the film cooling performance under various blowing ratios.

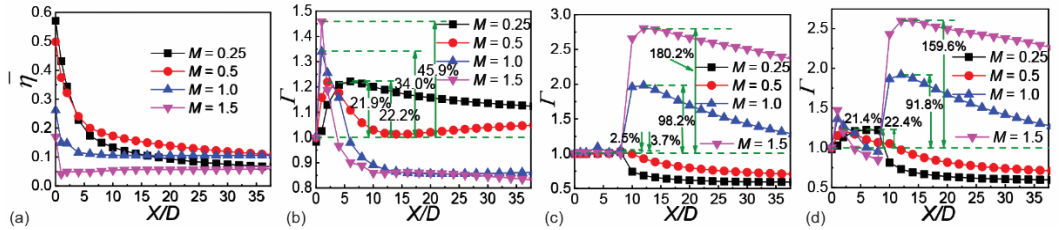

Figure 10. Comparisons of spanwise average film cooling effectiveness, $\bar{\eta}$, and dimensionless spanwise average effectiveness, Γ, in different actuators arrangement downstream the wall; (a) PA-off, (b) PA-up, (c) PA-down, and (d) PA-both

Figure 11 presents the average wall film cooling effectiveness under different actuator arrangements. This physical quantity is calculated based on a region with a spanwise range of –1.5*D* to 1.5*D* and a streamwise range of 0 to 38*D*. Under low blowing ratios, a slight improvement of the film cooling effectiveness is observed in the PA-up case. Compared with the PA-off case, the PA-up case shows 11.7% and 3.5% higher average wall film cooling effectiveness under blowing ratios of 0.25 and 0.5. Under high blowing ratios, the PA-down and PA-both significantly promote the film cooling performance. Compared with the PA-off case under blowing ratios of 1.0 and 1.5, the PA-down case has 48.8% and 138.3% increases in the average effectiveness, and the PA-both case increases by 46.6% and 122.9%. These consequences reveal that the film cooling performance deteriorates both in the PA-up case under high blowing ratios and in the PA-down case and PA-both case at low blowing ratios. This is because the PA-up case decreases the momentum of the coolant air near the film cooling hole under high blowing ratios, and the total momentum of the downstream coolant air is less than that of PA-off case. With entrainment of high temperature mainstream, the height of the coolant air downstream the wall increases. The coolant air adheres to the wall well, and the PA-down case and PA-both case cause rebounds of the fluid near the wall at low blowing ratios.

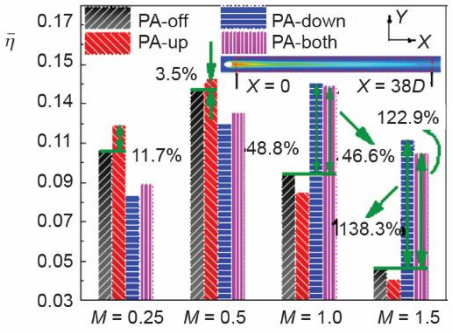

Figure 11. Average wall film cooling effectiveness downstream the wall for different actuator arrangements

Figure 12 shows vortex structures by *Q* criterion for film holes in different cases, including horseshoe vortex and counter-rotating vortex pair (CRVP). When the coolant air rolls

up close to the hole outlet, the horseshoe vortex is formed and the CRVP is formed in the shear layer on both sides of the coolant air. The CRVP indicates mixing degree of mainstream and coolant air. Compared with the PA-off case, scale of vortex in the PA-up case reduces. When the plasma actuator is arranged downstream the wall, the vortices near the hole increase, but the CRVP behind the actuator collapses. These results reveal that when a plasma actuator is applied, size of vortex structures reduces effectively and mixing effect of mainstream with coolant air weakens. Heat transfer between blade and coolant air is effectively improved.

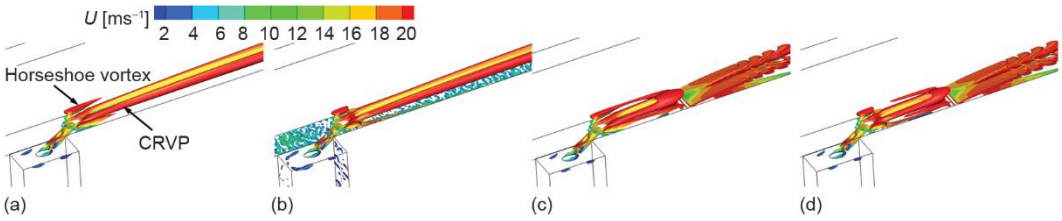

Figure 12. Vortex structure of gas film hole by *Q* criterion, *M* = 1.0; (a) PA-off, (b) PA-up, (c) PA-down, and (d) PA-both

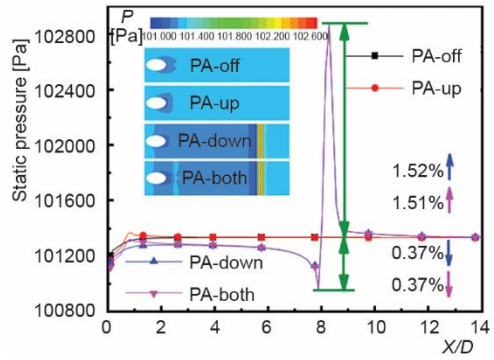

Figure 13. Pressure distribution of wall centerline, *M* = 1.0

Figure 13 presents pressure distributions on wall centerlines in different actuator arrangements. When the plasma actuator is placed at the hole outlet, the pressure on the wall is less than that without actuator. This result is because large jet velocity of coolant air near hole outlet weakens aerodynamic induction effect of plasma actuation. Wall pressure changes suddenly when plasma actuator is placed downstream a wall. The downstream fluid impinges on wall surface, which causes a significant pressure difference. In the PA-down and PA-both cases, static pressure before $X = 8D$ is less than that in the PA-off case. Static pressures near the position of $X = 8D$ in the PA-down case show two extremes which are 0.37% below and 1.52% above those in the PA-off case. Velocities in cases with actuators are much higher than those in cases without actuators, which further proves wall-jet actuation of plasma according to Bernoulli equation in [21]:

$$p + \frac{1}{2}\rho v^2 + \rho g h = \text{constant} \tag{14}$$

Conclusions

In this paper, flow characteristics and film cooling performance were numerically investigated by analyzing effects of blowing ratio and plasma placement of plasma actuation. The primary conclusions are shown as follows.

- Plasma aerodynamic actuation reduces outlet momentum of coolant air, which enhances adhesion performance of coolant air. After the plasma is applied, the velocity boundary layer nearby the wall becomes thinner. The plasma actuator is easily used to control the fluid flow.

- Film cooling performance is significantly improved with plasma actuator located downstream the film hole under high blowing ratios of 1.0 and 1.5 or plasma actuator arranged near the film hole under low blowing ratios of 0.25 and 0.5. Compared with plasma off, the average wall film cooling effectiveness of the PA-up case increases by 11.7% and 3.5% blowing ratios of 0.25 and 0.5, and the average wall cooling effectiveness of the PA-down and PA-both increases by 138.3% and 122.9% under blowing ratio of 1.5. The film cooling performance downstream the wall is deteriorated for the PA-up case under high blowing ratios of 1.0 and 1.5, and for the PA-down case and the PA-both case under low blowing ratios of 0.25 and 0.5.
- With plasma inducing, weakening effect on vortex structures is more significant, and effect on airflow disturbance strengthens with actuators downstream the wall. The actuation causes two sharp extremums of wall pressure, and the maximum wall pressure difference of 1.89% is obtained in the PA-down case.

Acknowledgment

This work is supported by the Natural Science Foundation of Hebei Province of China (Grant No. E2021202163), the Special Project of Science and Technology Winter Olympics in the Hebei Technology Innovation Guidance Plan (Grant No. 21474501D), the Project of Innovation Ability Training for Postgraduate Students of Education Department of Hebei Province (Grant No. CXZZSS2021046), and the Foundation of Key Laboratory of Thermo-Fluid Science and Engineering (Xi'an Jiaotong University), Ministry of Education, Xi'an 710049, P.R. China (Grant No. KLTFSE2018KFJJ01).

Nomenclature

a – vertical height of plasma region, [mm]
b – streamwise length of plasma region, [mm]
D – diameter of film cooling hole, [mm]
DR – coolant air to mainstream density ratio ($= \rho_c/\rho_\infty$), [–]
E – electric field intensity, [kVcm^{-1}]
E_b – breakdown electric field intensity, [kVcm^{-1}]
e_c – elementary charge, [C]
F – body force, [mNmm^{-3}]
f – frequency of applied voltage, [kHz]
k_1, k_2 – spatial distribution coefficient of the electric field, [–]
L – length of film hole, [mm]
L_1 – width of exposed electrode, [mm]
L_2 – width of covered electrode, [mm]
L_3 – spanwise length of the electrode, [mm]
M – blowing ratio ($= DRU_c/U_\infty$), [–]
s – spacing between the electrodes, [mm]
T – local fluid temperature, [K]
Δt – charge time of plasma, [μs]
U – streamwise velocity of jet flow, [ms^{-1}]
W – normal velocity of jet flow, [ms^{-1}]
X, Y, Z – coordinate direction distance, [mm]

Greek symbols

Γ – dimensionless average film cooling, [–]
η – film cooling effectiveness, [–]
$\overline{\eta}$ – average cooling effectiveness, [–]
Θ – dimensionless temperature, [–]
ρ_c – charge density, [Cm^{-3}]
φ – applied voltage, [kV]

Subscripts

aw – adiabatic wall
c – coolant air
∞ – mainstream

Acronyms

CRVP – counter rotating vortex pairs
SDBD – surface dielectric barrier discharge
STPA – saw-tooth plasma actuator
PA – plasma actuator

References

[1] Tian, K., *et al.*, Effect of Blockage Configuration on Film Cooling with and without Mist Injection, *Energy*, *153* (2018), June, pp. 661-670
[2] Zhang, B., *et al.* Experimental Investigation of Geometrical Effect on Flow and Heat Transfer Performance of Lamilloy Cooling Structure, *Thermal Science*, *24* (2020), 3A, pp. 1835-1843

[3] Wang, J., *et al.*, Effects of Hole Configuration on Film Cooling Effectiveness and Particle Deposition on Curved Surfaces in Gas Turbines, *Applied Thermal Engineering*, *190* (2021), May, ID 116861
[4] He, J., *et al.*, Film Cooling Performance Enhancement by Upstream V-Shaped Protrusion/Dimple Vortex Generator, *International Journal of Heat and Mass Transfer*, *180* (2021), Dec., ID 121784
[5] Tian K., *et al.*, Effect of Combined Hole Configuration on Film Cooling with and without Mist Injection, *Thermal Science*, *22* (2018), 5, pp. 1923-1931
[6] Ravi, D., *et al.*, Enhancing Film Cooling Effectiveness in a Gas Turbine End-Wall with a Passive Semi Cylindrical Trench, *Thermal Science*, *23* (2019), 3B, pp. 2013-2023
[7] Rodrigues, F. F., *et al.*, Experimental Analysis of Dielectric Barrier Discharge Plasma Actuators Thermal Characteristics under External Flow Influence, *ASME Journal of Heat Transfer*, *140* (2018), 10, ID 102801
[8] Moreau, E., Airflow Control by Non-Thermal Plasma Actuators, *Journal of Physics D: Applied Physics*, *40* (2007) 4, pp. 605-636
[9] Audier, P., *et al.*, Film Cooling Effectiveness Enhancement Using Surface Dielectric Barrier Discharge Plasma Actuator, *International Journal of Heat and Fluid Flow*, *62* (2016), Part B, Dec, pp. 247-257
[10] Dai, S. J., *et al.*, An Experimental Study of Plasma Aerodynamic Actuation on a Round Jet in Cross Flow, *AIP Advances*, *5* (2015), 3, ID 037143
[11] Li, G. Z., *et al.*, Numerical Comparison of Saw-Tooth Plasma Actuators for Film Cooling Flow Control over a Flat Plate, *International Journal of Thermal Sciences*, *163* (2021), May, ID 106807
[12] Li, G. Z., *et al.*, Large Eddy Simulation of Film Cooling Effectiveness on a Turbine Vane Pressure Side with a Saw-Tooth Plasma Actuator, *Aerospace Science and Technology*, *112* (2021), May, ID 106615
[13] Zhang, X., *et al.*, Leading-Edge Flow Separation Control over an Airfoil Using a Symmetrical Dielectric Barrier Discharge Plasma Actuator, *Chinese Journal of Aeronautics*, *32* (2019), 5, pp. 1190-1203
[14] Schatzman, D. M., Thomas, F. O., Turbulent Boundary-Layer Separation Control with Single Dielectric Barrier Discharge Plasma Actuators, *AIAA Journal*, *48* (2010), 8, pp. 1620-1634
[15] Hu, X., *et al.*, Experimental Study of Rotor Flow Separation Control Using a New Type of Dielectric Barrier Discharge Plasma Actuator, *Journal of Thermal Sciences*, *28* (2018), Mar., pp. 354-359
[16] Shyy, W., *et al.*, Modeling of Glow Discharge-Induced Fluid Dynamics, *Journal of Applied Physics*, *92* (2002), 11, pp. 6434-6443
[17] Goldstein, R. J., *et al.*, Effects of Hole Geometry and Density on Three-Dimensional Film Cooling, *International Journal of Heat and Mass Transfer*, *17* (1974), 5, pp. 595-607
[18] Silva C., and Pereira J., Invariants of the Velocity-Gradient, Rate-of-Strain, and Rate-of-Rotation Tensors across the Turbulent/Nonturbulent Interface in Jets, *Physics of Fluids*, *20* (2008), 5, ID 055101
[19] Wang, J., *et al.*, Effect and Optimization of Backward Hole Parameters on Film Cooling Performance by Taguchi Method, *Energy Conversion and Management*, *214* (2020), June, ID 112809
[20] Sinha, A. K., *et al.*, Film-Cooling Effectiveness Downstream of a Single Row of Holes with Variable Density Ratio, *ASME Journal of Turbomachinery*, *113* (1991), 3, pp. 442-449
[21] Hauptmann, E. G., *Fluid Flow: A First Course in Fluid Mechanics*, Macmillan, London, UK, 1971

Paper submitted: January 15, 2022
Paper revised: February 9, 2022
Paper accepted: March 28, 2022